Available online at www.sciencedirect.com
SCIENCE DIRECT®
Journal of Solid State Chemistry 172 (2003) 327–338
JOURNAL OF SOLID STATE CHEMISTRY
http://elsevier.com/locate/jssc

Characterization of the new $Bi_{\sim 6.2}Cu_{\sim 6.2}O_8(PO_4)_5$ oxyphosphate; a disordered compound containing 2- and 3-O(Bi, Cu)$_4$ tetrahedra—wide polycationic ribbons

El Mostafa Ketatni,[a] Marielle Huvé,[b] Francis Abraham,[b] and Olivier Mentré[b,*]

[a] *Laboratoire d'Electrochimie et Chimie des Matériaux, Faculté des Sciences et Techniques, Université Cadi Ayyad, B.P. 523, Béni Mellal, Morocco*
[b] *Laboratoire de Cristallochimie et Physicochimie du Solide, UMR CNRS 8012, ENSCL, Université des Sciences et Technologies de Lille, B.P. 108, 59652 Villeneuve d'Ascq Cedex, France*

Received 28 May 2002; received in revised form 17 September 2002; accepted 7 October 2002

Abstract

The present work is dedicated to the XRD, ED and HREM characterization of a new bismuth copper oxyphosphate $Bi_{\sim 6.2}Cu_{\sim 6.2}O_8(PO_4)_5$ ($a = 11.599(2)$ Å, $b = 5.218(1)$ Å, $c = 37.541(5)$ Å, $R_1 = 0.0755$, $Rw_2 = 0.174$, G.S $Pn2_1a$). The relatively long size of its c parameter is due to the arrangement along this direction of two kinds of ribbon-like polycations formed by edge sharing O(Bi, Cu)$_4$ tetrahedra. The existence of such cations is characterized by the $b \sim 5.2$ Å value intrinsic to the ribbons structure and commonly found in bismuth oxyphosphate materials. In the title compound, 2-tetrahedra wide $[Bi_{\sim 2.4}Cu_{\sim 3.6}O_4]^{6.4+}$ and 3-tetrahedra wide $[Bi_{\sim 5}Cu_{\sim 3}O_6]^{9+}$ ribbons are isolated by phosphate groups and alternate along c. The interstitial site created between two different sizes ribbons is occupied by Cu^{2+} cations disordered over several close crystallographic sites. The mixed Bi^{3+}/Cu^{2+} nature of certain edge-of-ribbons positions induces a disorder over several configurations of the phosphate groups. The concerned oxygen atoms form the environment of the disordered interstitial Cu^{2+} cations which occupy tunnels formed by the phosphate anions. The high-resolution electron microscope study enables a precise correlation between the observed images and the refined crystal structure, evidencing the polycations visualization. Furthermore, this material being the second example of partially disordered compound similar chemical system, some topological rules can be deduced. The b-axis doubling was observed by ED and HREM and is assigned to the ordering of interstitial Cu^{2+} within tunnels cations. A partial intra-tunnel ordering was also observed.

1. Introduction

A number of $Bi^{III}/X^{V}/M^{II}$ oxides, X=P, V, As containing various divalent M^{II} cations have been reported during the last decade, e.g., $Bi_4Cu_3O_6(XO_4)_2$ [1,2], $BiM_2O_2(XO_4)$ [3–15], $BiMO(PO_4)$ [16–18]. For several reasons related to potential applications due to the Bi^{3+} $6s^2$ lone pair possessing cation (ionic conductivity, non-linear optical properties, ferroelectricity, etc.), these compounds are still currently being investigated, i.e., the very recent introduction of Mn^{2+} cations in $BiMn_2XO_6$ (X=P, V, As) [19] and $BiMnPO_5$ [20]. Almost all of them were commonly described by the association of isolated XO_4 groups sharing corners with MO_x polyhedra. In this description, the Bi^{3+} cations play an interstitial role within the created framework. This ionic-only Bi^{3+} function is rigorously incorrect and the Bi^{3+} coordination should be considered. As an example, $BiM_2O_2(XO_4)$ possesses $[BiO_2]^-$ infinite chains while $Bi_4Cu_3O_6(XO_4)_2$ shows $[Bi_2O_3]$ chains growing along a common lattice parameter, of about 5.2–5.5 Å. Therefore, such a model does not allow an obvious topological relationship between the several structures listed above and additional chemically related materials despite common geometric lattice features. Furthermore, new materials, namely $Bi_{\sim 1.2}M_{\sim 1.2}PO_{5.5}$ (M=Mn, Co, Zn) were prepared afterwards and structurally characterized showing evidence of a well-located Bi/M/O framework and high PO_4/M disorder in the formed cavities [21]. The framework is characterized by mixed Bi^{3+}/M^{2+} occupancy of certain sites responsible for the disordered interstitial space. The disorder is evidenced by statistic disorder over a number of

*Corresponding author. Fax: 33-03-20-43-68-14.
E-mail address: mentre@ensc-lille.fr (O. Mentré).

0022-4596/03/$ - see front matter © 2003 Elsevier Science (USA). All rights reserved.
doi:10.1016/S0022-4596(02)00080-4

superimposed M^{2+} positions and the several $(PO_4)^{3-}$ configurations slightly tilted or shifted from each other located over a multitude of residual electron density maxima. It avoids a proper visualization of the MO_x/PO_4 polyhedral linkage. The use of an original descriptive concept based on phosphate groups and complex infinite bidimensional ribbon-like polycations growing along the ~5.2 Å orthorhombic axis common to all the cited materials leads to the essential structural features of these materials and enables to establish a relationship between all the isolated materials, disordered or not. The polycations are built from oxygen-centered O(Bi, M)$_4$ tetrahedra sharing edges to form infinite ribbons of n tetrahedra width. The n number is the key to our new classification, varying from 1 (chains in BiMPO$_5$), to 2 (ribbons in BiM_2PO$_6$), 3 (ribbons in $Bi_{\sim 1.2}M_{\sim 1.2}PO_{5.5}$ and $Bi_4Cu_3O_6(XO_4)_2$),…, ∞ ($[Bi_2O_2]^{2+}$ plane of the Aurivilius series). The disorder or order evidenced in the prepared compounds appear to be a direct consequence of the mixed Bi/M or unique occupancy of the ribbons peripheral sites. Moreover, the refinement of X-ray patterns for several BiM_1Cd$_1$PO$_6$ compositions yield to the orthorhombic $a \sim a_{BiM_2XO_6} \sim$ 11.5 Å, $b \sim b_{BiM_2XO_6} \sim 5.5$ Å and c depending on the M nature (15.3 Å for M = Ni, 23.3 Å for M = Co, Zn and 37.5 Å for M = Cu). These results strongly suggest a monodimensional topological recombination that may involve the coexistence of ribbons of different width in the same structure and opens a wide field for future investigation. We hereby confirm this possibility by describing the synthesis, crystal structure and electron microscope study of the $Bi_{\sim 6.2}Cu_{\sim 6.2}O_8(PO_4)_5$ with $a = 11.599(2)$ Å, $b = 5.218(1)$ Å, $c = 37.541(5)$ Å, $R_1 = 0.0755$, $Rw_2 = 0.174$. Its crystal structure is formed from both 2- and 3-tetrahedra wide ribbons that ordered along the c-axis showing the reason for using the polycationic description model.

2. Experimental

2.1. Sample preparation

Single crystals of the title compound were obtained from heating at 980°C and slow cooling until room temperature (sweep = 3°C/h) of a 1 BiPO$_4$–3/2 CuO mixture. A green needle-shaped single crystal was selected and isolated from the inhomogeneous melt. The crystal structure refinement led to the nominal formula $Bi_{6.20}Cu_{6.20}O_8(PO_4)_5$ but considering disorder over several sites the approximate $Bi_{\sim 6.2}Cu_{\sim 6.2}O_8(PO_4)_5$ formula appears better adapted.

Single crystal X-ray diffraction data were collected on a Bruker SMART CCD- 1 K detector diffractometer (50 kV × 40 mA, Mo$K\alpha$-graphite monochromator) under the following conditions. A full reciprocal sphere corresponding to a total of 3 × 600 frames was collected (ω-scan, 40 s per frame, 0.3° oscillations for three different values of φ) at a crystal to detector distance of 45 mm. The intensity data were then extracted from the collected frames using the program SaintPlus 6.02 [22]. A Gaussian-type absorption correction, based on the precise faces indexation was then applied using the program Xprep of the SHELXTL package with, in first stage an approximate μ and finally the exact absorption coefficient deduced from the last refinement. Data were then corrected for the glass fiber and the area detector absorption using non-theta-dependent empirical corrections ($\mu r = 0$) with the program SADABS [23]. The pertinent data of the reflections collection, treatment and refinement are summarized in Table 1.

The pure powder was prepared from a stoichiometric mixture of $(NH_4)_2HPO_4$, CuO and Bi_2O_3 heated at

Table 1
Crystal data, measurement, and structure refinement parameters for $Bi_{6.2}Cu_{6.2}O_8(PO_4)_5$

Crystal data	
Crystal symmetry	Orthorhombic
Space group	$Pn2_1a$
Cell dimension (Å)	$a = 11.599(2)$ Å
	$b = 5.218(1)$ Å
	$c = 37.541(5)$ Å
Volume (Å)	2272.1(7) Å^3
Z	4
Data collection	
Equipment	Bruker SMART CCD
λ (Mo$K\alpha$ (graphite monochromator)) (Å)	0.7107
Density calc./meas.	6.65/6.70 g/cm^3
Color	Green
Scan mode	ω
θ range (°)	4.75–27
Recording reciprocal space	$-14 \leqslant h \leqslant 14, -6 \leqslant k \leqslant 6, -48 \leqslant l \leqslant 48$,
Number of measured reflections	12,671
Number of independent reflections	4396
μ(mm^{-1})(for $\lambda K\alpha = 0.7107$Å)	51.9
Limiting faces and distances (mm) from an arbitrary origin	$\bar{1}\,0\,\bar{2}$ 0.025
	$2\,\bar{4}\,\bar{1}$ 0.092
	$\bar{1}\,3\,\bar{3}$ 0.096
	$1\,0\,2$ 0.031
	$\bar{1}\,0\,2$ 0.031
	$1\,0\,\bar{2}$ 0.025
Merging R factor	0.027–0.150
Refinement	
Number of refined parameters	242
Refinement method	Least square on F^2
$R_1(F)[I > 2\sigma I]/R_1(F)$ [all data]	0.0755/0.0883
$wR_2(F^2)[I > 2\sigma I]/wR_2(F^2)$ [all data]	0.174/0.183
$w = 1/(\sigma^2(F_o^2) + (0.0493P)^2 + 9,2976P)$ with $P = (F_o^2 + 2F_c^2)/3$	
GooF	1.158
Max/Min $\Delta\rho$ (e Å^{-3})	0.72/0.01 e Å^{-3}

800°C for 48 h. Several intermediate grindings at 150°C, 300°C and 500°C were necessary to achieve complete reaction leading to a single phase. The purity was checked by powder X-ray diffraction using a BRUKER-D5000 diffractometer. The least-squares refined orthorhombic lattice parameters, $a = 11.599(2)$ Å, $b = 5.218(1)$ Å, $c = 37.541(5)$ Å, $F_{30} = 28(0.0113, 96)$, confirm the similarity with the studied single crystal. They were used for inter-atomic distance calculations. The indexed and refined powder pattern is given in Table 2.

Electron diffraction (ED) patterns and high-resolution images were obtained on a Jeol 200CX and a Jeol 4000EX with a point resolution of 1.7 Å. In each case, the material was crushed and dispersed on a holey carbon film deposited on a Cu grid. The computer simulated HREM images were calculated using Mac Tempas program [24].

The experimental density measured using a Micromeritics Accupyc 1330 Helium pycnometer yields $d_{exp} = 6.65(1)$ matching rather well with the 6.70 g/cm^3 calculated value. Because of the ambiguity about the real space group during the crystal structure determination a second harmonic generation (SHG) test was

Table 2
X-ray powder pattern for $Bi_{6.2}Cu_{6.2}O_8(PO_4)_5$

$h\,k\,l$	d_{obs} (Å)	d_{cal} (Å)	I/I_0	$h\,k\,l$	d_{obs} (Å)	d_{cal} (Å)	I/I_0
1 0 3	8.512	8.507	78.9	4 1 8	2.229	2.230	13.3
1 0 4	7.307	7.296	6.7	4 0 11	2.209	2.210	11.1
1 0 5	6.295	6.303	5.5	4 1 9	2.166	2.166	6.6
2 0 0	5.800	5.799	35.7	3 2 2	2.148	2.149	7.5
2 0 2	5.537	5.541	5.2	5 0 7	2.130	2.129	10.5
1 0 7	4.872	4.868	14.3	4 0 13	2.045	2.046	7.6
1 1 2	4.608	4.613	6.8	2 1 16		2.008	
1 1 3	4.453	4.448	5.0		2.008		7.0
1 1 4	4.247	4.244	5.9	5 1 6		2.008	
1 1 5	4.018	4.020	20.7	4 2 1	1.938	1.937	27.1
2 1 0	3.881	3.879	7.8	6 0 0	1.933	1.933	10.0
1 1 6	3.790	3.788	20.1	4 2 3	1.917	1.918	10.5
0 0 10	3.752	3.754	11.4	4 0 15	1.895	1.895	10.4
3 0 3	3.695	3.694	17.3	0 0 20	1.876	1.877	6.3
3 0 4	3.575	3.575	10.6	5 1 10	1.845	1.846	6.6
1 1 7	3.560	3.560	8.2	4 0 16		1.824	
2 1 5	3.445	3.446	5.6		1.824		20.2
1 0 11	3.276	3.274	9.8	4 2 7		1.824	
2 1 0	3.150	3.151	22.3	5 0 13	1.809	1.809	10.6
2 1 7	3.143	3.143	20.0	2 0 20	1.786	1.786	6.6
2 1 8	2.989	2.990	100	6 1 5	1.762	1.762	7.6
4 0 0	2.899	2.900	39.8	5 1 12	1.754	1.755	21.9
3 1 5	2.870	2.871	42.6	0 3 1	1.737	1.738	8.9
1 0 13	2.803	2.802	54.5	5 2 2	1.726	1.726	11.9
3 1 6	2.782	2.782	19.9	6 1 7		1.717	
2 0 12	2.752	2.753	16.5		1.717		12.2
3 1 7	2.688	2.688	8.8	5 2 3		1.717	
0 2 0	2.608	2.609	72.2	2 1 20	1.690	1.690	9.5
20 13		2.585		5 2 6		1.671	
	2.586		10.0		1.671		8.4
0 2 2		2.584		2 2 16		1.671	
4 1 0	2.536	2.535	10.8	6 1 9	1.663	1.663	8.8
1 2 3	2.493	2.495	8.5	7 0 7	1.584	1.583	4.8
4 1 5	2.401	2.402	4.9	7 1 2		1.574	
2 2 1	2.375	2.375	5.7		1.574		14.2
0 0 16	2.347	2.346	27.3	3 3 3		1.574	
3 0 13	2.314	2.314	13.9	0 0 24	1.564	1.564	13.6
2 0 15	2.299	2.298	12.5	33 5		1.552	
0 2 8		2.280			1.552		15.3
	2.282		11.4	6 2 1		1.552	
5 0 3		2.281					

Table 3
Atomic positions and isotropic equivalents of temperature factors for $Bi_{6.20}Cu_{6.20}O_8(PO_4)_5$

Atom	Occ.	x	y	z	U_{eq} (Å^2)
Bi(1)		0.07595(8)	0.25000	0.62314(3)	0.0165(3)
Bi(2)		−0.15041(8)	−0.2498(8)	0.62181(3)	0.0157(3)
Bi(3)		−0.14280(9)	0.2496(8)	0.69402(3)	0.0174(3)
Bi(4)		0.07769(9)	−0.2519(7)	0.69548(3)	0.0173(3)
Bi(5)		0.39165(8)	−0.2497(8)	0.50165(3)	0.0170(3)
Bi(6)		0.06607(9)	−0.2509(8)	0.55318(3)	0.0210(3)
Cu/Bi(7)	0.8/0.2	0.5952(2)	−0.2563(14)	0.43369(8)	0.030(2)
Cu(2)		0.6029(3)	−0.2508(19)	0.55780(9)	0.0208(9)
Cu(3)		0.0420(3)	0.2420(18)	0.76112(9)	0.0194(9)
Cu(4)		−0.1035(3)	−0.7573(19)	0.55236(9)	0.0203(9)
Cu(5)		0.3754(4)	−0.2464(18)	0.74541(10)	0.029(1)
Cu(6)	0.489	0.5307(7)	0.724(3)	0.3484(2)	0.026(3)
Cu(7)	0.49	0.527(2)	0.014(5)	0.3492(6)	0.087(9)
Cu(8)	0.42	0.5305(9)	0.429(2)	0.3419(3)	0.007(4)
O(1)		−0.034(3)	0.012(8)	0.6605(10)	0.023(9)
O(2)		−0.041(2)	−0.980(5)	0.5861(7)	0.006(6)
O(3)		−0.039(5)	0.006(9)	0.7288(12)	0.053(13)
O(4)		0.497(4)	−0.002(8)	0.5353(9)	0.02(1)
O(5)		−0.026(3)	0.494(5)	0.7299(7)	0.004(6)
O(6)		−0.039(3)	−0.477(7)	0.5849(9)	0.025(9)
O(7)		−0.028(2)	0.509(6)	0.6570(7)	0.004(6)
O(8)		0.502(3)	−0.496(6)	0.5358(7)	0.006(8)
P(1)		−0.3249(6)	−0.766(3)	0.6002(2)	0.0179(16)
O(9)		−0.2403(17)	−0.772(8)	0.6310(6)	0.023(5)
O(15)		−0.303(2)	−0.487(5)	0.5789(7)	0.016(6)
O(16)		−0.4499(18)	−0.788(7)	0.6110(6)	0.025(6)
O(17)		−0.291(3)	−0.929(6)	0.5747(8)	0.029(8)
P(2)		−0.1671(6)	−1.212(2)	0.4983(2)	0.0107(18)
O(10)		−0.2937(17)	−1.234(9)	0.4996(5)	0.023(5)
O(14)		−0.1141(17)	−1.277(7)	0.4611(5)	0.021(5)
O(18)		−0.144(2)	−0.940(5)	0.5115(7)	0.018(5)
O(19)		−0.105(3)	−1.402(6)	0.5231(8)	0.034(7)
P(3)		0.1373(7)	−0.279(3)	0.8071(2)	0.0176(19)
O(11)		0.2698(17)	−0.244(10)	0.8115(5)	0.025(5)
O(20)		0.084(3)	−0.009(4)	0.7969(8)	0.039(8)
O(21)		0.108(4)	−0.453(8)	0.7742(8)	0.091(15)
O26)		0.083(3)	−0.370(7)	0.8435(6)	0.070(12)
P(4)		0.2829(8)	−0.767(4)	0.7044(3)	0.035(2)
O(12)		0.173(2)	−0.767(11)	0.6830(7)	0.050(4)
O(22)		0.299(3)	−1.022(7)	0.7154(10)	0.050(4)
O(25)		0.384(3)	−0.716(8)	0.6739(7)	0.050(4)
O(27)		0.271(3)	−0.564(6)	0.7339(8)	0.050(4)
P(5)		0.7043(8)	−0.717(3)	0.3979(3)	0.028(2)
O(13)		0.832(3)	−0.758(12)	0.3881(8)	0.058(5)
O(23)		0.691(3)	−0.913(6)	0.428(1)	0.058(5)
O(24)		0.632(3)	−0.834(6)	0.3690(8)	0.058(5)
O(28)		0.668(3)	−0.436(4)	0.3997(10)	0.058(5)

performed at the University of Houston Department of Chemistry (see acknowledgements) on a small amount of polycrystalline material with a modified Kurtz-NLO system [25] using a 1064 nm light (for details on the experiment see Refs. [26,27]. It shows a SHG efficient signal corresponding to a non-centrosymmetric space group.

2.2. Single crystal X-ray structure analysis

The crystal structure refinement was performed using the SHELXL program in both the *Pnma* and $Pn2_1a$ space groups predicted by the observed $0\,k\,l{:}k+l=2n$ and $h\,k\,0{:}h=2n$ conditions. The systematic extinctions were unambiguously verified on the powder sample by ED as reported below. Therefore, considering the SHG positive test, only $Pn2_1a$ appears to be available. Six bismuth atoms and five copper atoms were located using the Patterson function calculation. Then five phosphorus atoms and three copper atoms appeared on the subsequent Fourier-difference maps. The Cu(6), Cu(7) and Cu(8) are superposed along the *b*-axis ($x\sim0.53$, y, $z\sim0.37$) but are too close from each other involving the refinement of their occupancies. They converge to values of around 0.5. The oxygen coordinating Bi(1)–Bi(7) and Cu(1) to Cu(6) appear at the same time. Then the PO_4 polyhedra apices were located. No major problem was met for P(1) and P(2) coordination anions even if the P(1)–O(15) distance of 1.68(3) is very suspicious and could picture a weak disorder around this cation. On the contrary, P(3)–P(5) show the clues typical of a strong statistical disorder over several configurations, even if we easily refined the predominant one. It is noteworthy that we had to use geometrical restraints based on P–O distances and O–P–O angles for some oxygen atoms of the latter phosphorus atoms. At that stage, a racemic twinning refinement, frequently observed for non-centrosymmetric crystals, improves the refinement (cryst.2/cryst.1 volume ratio = 0.44(3)). Because of its low U_{iso} value, one of the copper atoms ($x\sim0.59$, $y\sim0.75$, $z\sim0.43$) was considered as a mixed Bi/Cu site with respective occupancies refined to 0.204(6)/0.796(6) yielding a sensitive improvement of the convergence (1% loss in R_1). Then, the electroneutrality was assured by fixing the Cu(6) + Cu(7) + Cu(8) occupancies sum to the calculated value leading to $Occ._{Cu(6)} = 0.49(1)$, $Occ._{Cu(7)} = 0.49(2)$, $Occ._{Cu(8)} = 0.42(2)$. Finally, anisotropic thermal coefficients, optimization of the weighting scheme yield the final $R_1 = 0.0755$. As discussed below, a mixed Bi/Cu occupancy of the same crystallographic site could look very unlikely but was already encountered and largely discussed in Ref. [21]. Actually, it is the major reason for the Cu(6)/Cu(7)/Cu(8) disorder and for the $P(4)O_4$ and $P(5)O_4$ combination of several tilted configurations. Our goal in this work is to present the ideal crystal structure of the title compound and, even if they probably exist, it seems unrealizable to search for complementary ligand atoms around P(4) and P(5) considering the low final residual electronic density. Atomic positions, isotropic equivalents of temperature factors for $Bi_{6.20}Cu_{6.20}O_8(PO_4)_5$ are given in Table 3. Components of anisotropic temperature factors for Bi and Cu atoms are shown in Table 4.

2.3. Electron diffraction

To confirm the XRD results and to look for evidence of further ordering, the sample was studied by ED and high-resolution microscopy (HREM).

In the ED study the higher order Laue zones were taken into account, in order to check the existence of glide planes *n* and *a*, by comparison of the periodicity and the shifting between the zero-order Laue zone (ZOLZ) and first-order Laue zone (FOLZ). For the [100] and [010] ZAP, the FOLZ were obtained by tilting the crystal from the ZOLZ, because of the large reciprocal a^* and b^* values, while the ZOLZ and FOLZ appear on the same image for the [001] ZAP. The [001], [100] and [010] zone axis patterns (ZAP) are shown, respectively, in Figs. 1a–c.

In a first stage, we have been interested in the intense fundamental spots. In order to limit the size of Figs. 1b

Table 4
Anisotropic temperature factor components (in Å^2) for $Bi_{6.20}Cu_{6.20}O_8(PO_4)_5$

Atom	U_{11}	U_{22}	U_{33}	U_{12}	U_{13}	U_{23}
Bi(1)	0.0122(5)	0.0278(7)	0.0094(5)	−0.0040(13)	0.0029(4)	−0.0109(9)
Bi(2)	0.0116(5)	0.0279(7)	0.0076(5)	−0.0060(14)	−0.0009(4)	0.0014(11)
Bi(3)	0.0159(5)	0.0260(7)	0.0104(5)	−0.0057(14)	0.0035(4)	−0.0091(11)
Bi(4)	0.0113(5)	0.0285(7)	0.0120(5)	−0.0050(14)	−0.0014(4)	−0.0076(12)
Bi(5)	0.0106(5)	0.0277(7)	0.0127(5)	−0.0061(13)	−0.0026(4)	−0.0063(10)
Bi(6)	0.0165(5)	0.0338(8)	0.0127(6)	−0.0003(14)	0.0047(4)	−0.0117(11)
Cu/Bi(7)	0.0281(15)	0.032(2)	0.0282(15)	0.015(3)	−0.0074(12)	−0.005(3)
Cu(2)	0.0126(16)	0.036(3)	0.0144(18)	0.009(5)	−0.0043(13)	0.012(4)
Cu(3)	0.0136(16)	0.028(2)	0.0166(18)	0.004(4)	−0.0001(13)	−0.017(3)
Cu(4)	0.0230(18)	0.030(2)	0.0077(17)	−0.002(5)	−0.0048(14)	−0.013(3)
Cu(5)	0.036(2)	0.032(3)	0.018(2)	0.007(5)	−0.0139(16)	−0.003(4)

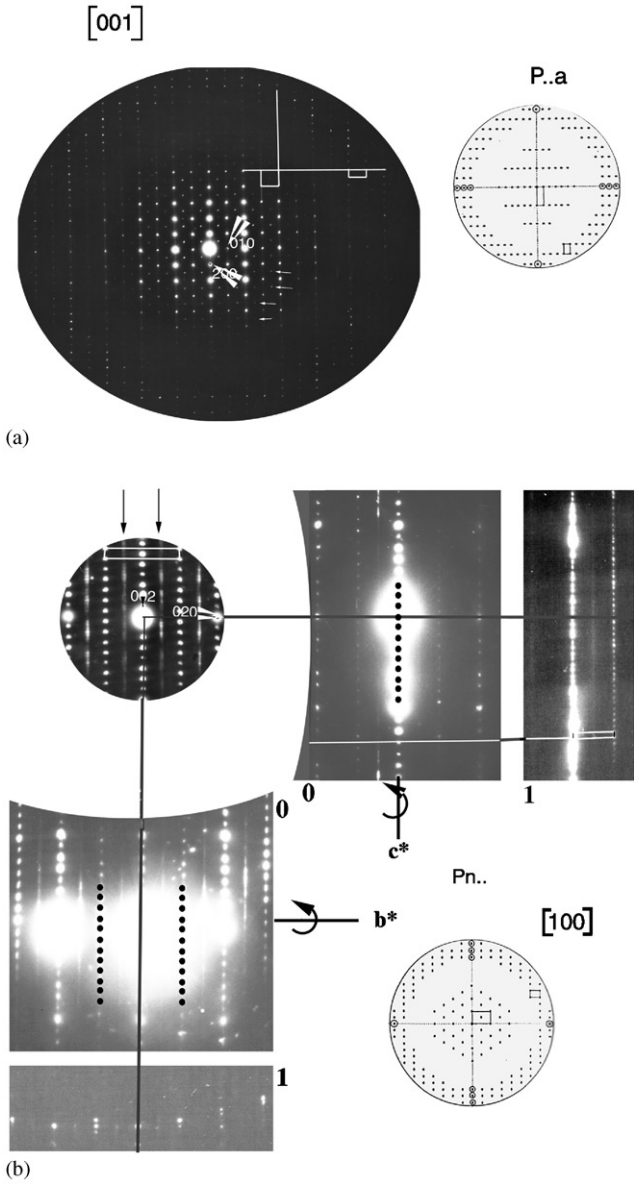

Fig. 1. (a) [001] and (b) [100] ZAP. A difference of periodicity but no shift were observed between the ZOLZ and FOLZ (for intense spots) according to the table [28] in part represented on the right part. (c) [010] ZAP. No shift nor difference of periodicity has been detected (for intense spots). Therefore, the partial extinction symbol is Pn-a (means no glide plan). Arrows indicate superstructure phenomena evidenced by (a) supplementary weaker spots (b) diffuse streaks (c) supplementary Laue zone.

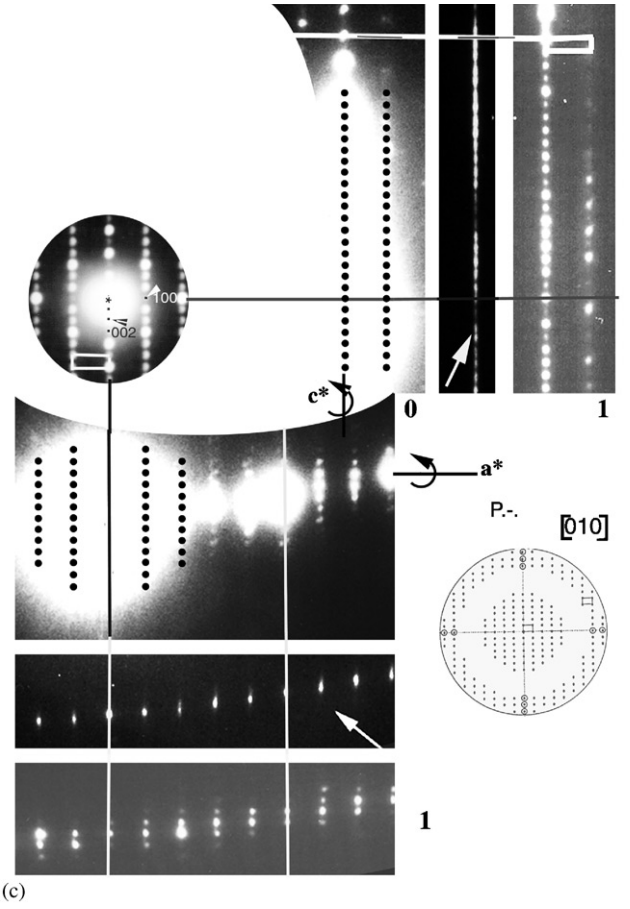

Fig. 1 (*continued*).

and c, the FOLZ and ZOLZ have been dissociated. For the [001] (Fig. 1a) and [100] (Fig. 1b) ZAP, a difference of periodicity but no shift were observed between the ZOLZ and FOLZ. For the [010] ZAP (Fig. 1c) no shift nor difference of periodicity was detected. It led to the partial extinction symbol Pn-a according to the table [28]. The line in the symbol indicates a lack of glide plane perpendicular to the *b* direction in that case. The violating $0\,k\,0$, $k = 2n+1$ and $0\,0\,l$, $l = 2n+1$ reflections, visible on the [001] ZOLZ and [100] ZOLZ, respectively, are generated by double diffraction since they disappear by tilting. These observations are in agreement with the $Pn2_1a$ space group used in the XRD investigation.

Superimposed on the basic intense spots some extra phenomena were observed: (i) supplementary weaker spots on [001] ZAP indicated by small white arrows in Fig. 1a; (ii) diffuse streaks parallel to the *c*-axis involving a *b*-doubling, on [100] ZAP. They are indicated by black arrows in Fig. 1b. The satellite spots observed in Fig. 1a correspond to the cross-sections of these diffuse lines; (iii) supplementary Laue zone on the [010] ZAP indicated by white arrows in Fig. 1c. The contrast of this latter Laue zone has been artificially enhanced to distinguish it easily. These observations led to establish a partial ordering phenomenon consisting in a multiplication of the *b* parameter by 2 strongly correlated to a disordered phenomenon along *c*. It implies that the X-ray crystal structure refinement refers to an average structure since satellite spots were not taken into account.

3. Results and discussion

3.1. Crystal structure description

Due to the strong disorder affecting both the metallic Cu(6)–Cu(7)–Cu(8) atoms, and the mixed Cu/Bi(7) occupancy, it appears rather complicate to describe the anionic environment of the cations and to describe the structure framework from the linkage of cation-centered coordination polyhedra through corners, edges and/or faces, as commonly utilized. We have recently developed a new descriptive concept for $Bi_{\sim 1.2}M_{\sim 1.2}PO_{5.5}$ (M = Zn, Co, Mn) which possess mixed Bi/M occupancy over most of their sites. Thus, a wide range of recently studied materials were re-analyzed on the basis of oxygen centered O(Bi, M)$_4$ tetrahedra and appear to exhibit a network built from one-dimensional ribbons of different width providing evidence for an unexpected topological relationship between a number of compounds. This coordination-type was applied to show evidence for regular tetrahedra around O(1)–O(8) anions with O–Bi/Cu distances in a 1.91–2.4 Å range, Table 5. These tetrahedra share their edges to form two kinds of polycationic ribbons growing along b and arranged along the c-axis. The short-ones, 2-tetrahedra wide, have stoichiometry $[Bi_{2.4}Cu_{3.6}O_4]^{6.4+}$ while the long-ones, 3-tetrahedra wide, have stoichiometry $[Bi_5Cu_3O_6]^{9+}$, Fig 2. Actually, similarly to $Bi_{\sim 1.2}$-$M_{\sim 1.2}PO_{5.5}$, every edge-of-ribbons sites, namely Cu(2), Cu(3), Cu(4), Cu(5), Bi(6) and Cu/Bi(7), are potentially available for mixed Bi^{3+}/Cu^{2+} occupancy. The assignment of their chemical nature is only based on single crystal diffraction refinement but it is obvious that a slight deviation from a Bi-only or Cu-only occupancy is reasonable. In that case the electroneutrality would be compensed by a slight change of the Cu(6/7/8) occupancies. The two kinds of ribbons alternate along c forming rows with –short–long–long– sequence. Along [100], polycations are separated by PO_4^{3-}groups and are shifted from each other according to the a-glide. The space liberated between consecutive long and short ribbons is occupied by phosphate groups which form tunnels guesting the Cu(6)/Cu(7)/Cu(8) cations, Fig. 3a. Thus, the interstitial copper cations form disordered chains parallel to b. Considering the crystal structure refinement, the developed formula is $[Bi_{2.4}Cu_{3.6}O_4]_1$ $[Bi_5Cu_3O_6]_2$ $Cu_{2.8}$ $(PO_4)_{10}$ but for reason developed above a more approximate formula appears better adapted.

It is rather interesting to recall that the $Bi_{\sim 1.2}M_{\sim 1.2}PO_{5.5}$ crystal structure can be described $[Bi_{4.8}M_{3.2}O_6]_1M_{1.6}(PO_4)_4$ using the same formalism, Fig. 3b. This material exhibits 3-tetrahedra wide ribbons-only with each of the metal ions sites at the edges of the ribbons partially occupied by Bi and M ions. As a consequence, the interstitial PO_4 and M cavities, appears strongly disordered. In the titled compound, fortunately, the disordered is sensitively reduced because of the unique nature of the edge-of-ribbons sites (at least at the XRD detection accuracy) for almost all of them, at XRD refinement precision, only the peripheral Cu/Bi(7) site adopts a mixed nature. Thus disorder is barely observed on P(3)O$_4$ and P(5)O$_4$. The complementary 2-tetrahedra wide ribbons are found in the generic BiM_2XO_6 materials, which are well-ordered because of the M^{2+}-only nature of the edges of the ribbons. Its structure is represented in Fig. 3c leading to $[Bi_2M_4O_4]_1(PO_4)_2$. It is easily observable that the $Bi_{6.2}Cu_{6.2}O_8(PO_4)_5$ crystal structure corresponds to the juxtaposition of these two latter compounds along c and can be considered as an intergrowth between both.

Table 5
Selected bond lengths (Å) for $Bi_{6.2}Cu_{6.2}O_8(PO_4)_5$

O(Bi/Cu)$_4$			
O(1)–Bi(1)	2.266(38)	O(2)–Bi(1)^{i}	2.283(25)
O(1)–Bi(2)	2.408(38)	O(2)–Bi(2)^{i}	2.321(25)
O(1)–Bi(3)	2.171(38)	O(2)–Bi(6)^{i}	2.251(25)
O(1)–Bi(4)	2.302(38)	O(2)–Cu(4)	1.865(27)
O(3)–Bi(3)	2.184(50)	O(4)–Bi(5)^{v}	2.308(41)
O(3)–Bi(4)	2.282(51)	O(4)–Bi(5)	2.182(41)
O(3)–Cu(3)	1.967(49)	O(4)–Cu(2)	1.977(43)
O(3)–Cu(5)^{ii}	1.912(50)	O(4)–Cu/Bi(7)^{v}	2.035(41)
O(5)–Bi(3)	2.297(30)	O(6)–Bi(1)^{i}	2.422(35)
O(5)–Bi(4)^{iii}	2.208(29)	O(6)–Bi(2)	2.235(35)
O(5)–Cu(5)^{iv}	2.00(3)	O(6)–Bi(6)	2.072(35)
O(5)–Cu(3)	1.930(29)	O(6)–Cu(4)	2.047(36)
O(7)–Bi(1)	2.213(27)	O(8)–Bi(5)	2.221(31)
O(7)–Bi(2)^{iii}	2.312(27)	O(8)–Bi(5)^{vi}	2.291(31)
O(7)–Bi(4)^{iii}	2.268(27)	O(8)–Cu(2)	1.921(33)
O(7)–Bi(3)	2.353(27)	O(8)–Cu/Bi(7)^{vi}	2.104(31)
PO$_4$			
P(1)–O(17)	1.340(33)	P(2)–O(10)	1.474(21)
P(1)–O(16)	1.510(22)	P(2)–O(18)	1.527(28)
P(1)–O(9)	1.517(23)	P(2)–O(19)	1.539(33)
P(1)–O(15)	1.68(3)	P(2)–O(14)	1.563(21)
P(3)–O(11)	1.556(22)	P(4)–O(22)	1.406(42)
P(3)–O(21)	1.570(37)	P(4)–O(12)	1.507(26)
P(3)–O(26)	1.578(28)	P(4)–O(27)	1.539(35)
P(3)–O(20)	1.585(28)	P(4)–O(25)	1.660(33)
P(5)–O(24)	1.501(34)		
P(5)–O(28)	1.527(27)		
P(5)–O(23)	1.532(37)		
P(5)–O(13)	1.541(37)		
Special distance Cu–Cu			
Cu(6)–Cu(7)^{ii}	3.705(30)		
Cu(6)–Cu(8)^{i}	3.687(19)		
Cu(7)–Cu(8)	3.065(28)		

Symmetry codes: (i) $x, -1+y, z$; (ii) $-0.5+x, y, 1.5-z$; (iii) $x, 1+y, z$; (iv) $-0.5+x, 1+y, 1.5-z$; (v) $1-x, 0.5+y, 1-z$; (vi) $1-x, -0.5+y, 1-z$.

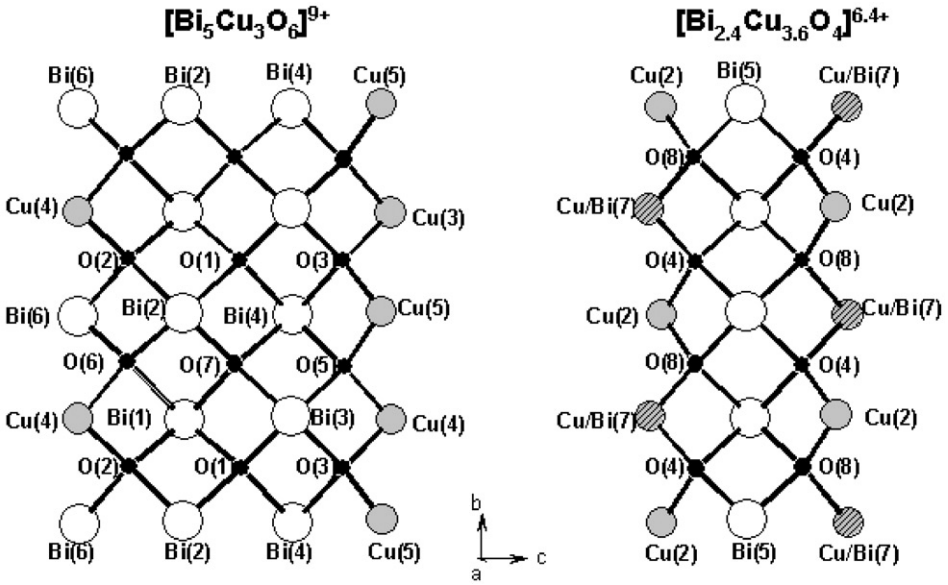

Fig. 2. The $[Bi_5Cu_3O_6]^{9+}$ ribbons (3-tetrahedra wide) and the $[Bi_{2.4}Cu_{3.6}O_4]^{6.4+}$ polycations (2-tetrahedra wide) with the label scheme. Each oxygen is tetrahedrally coordinated by Bi and U cations.

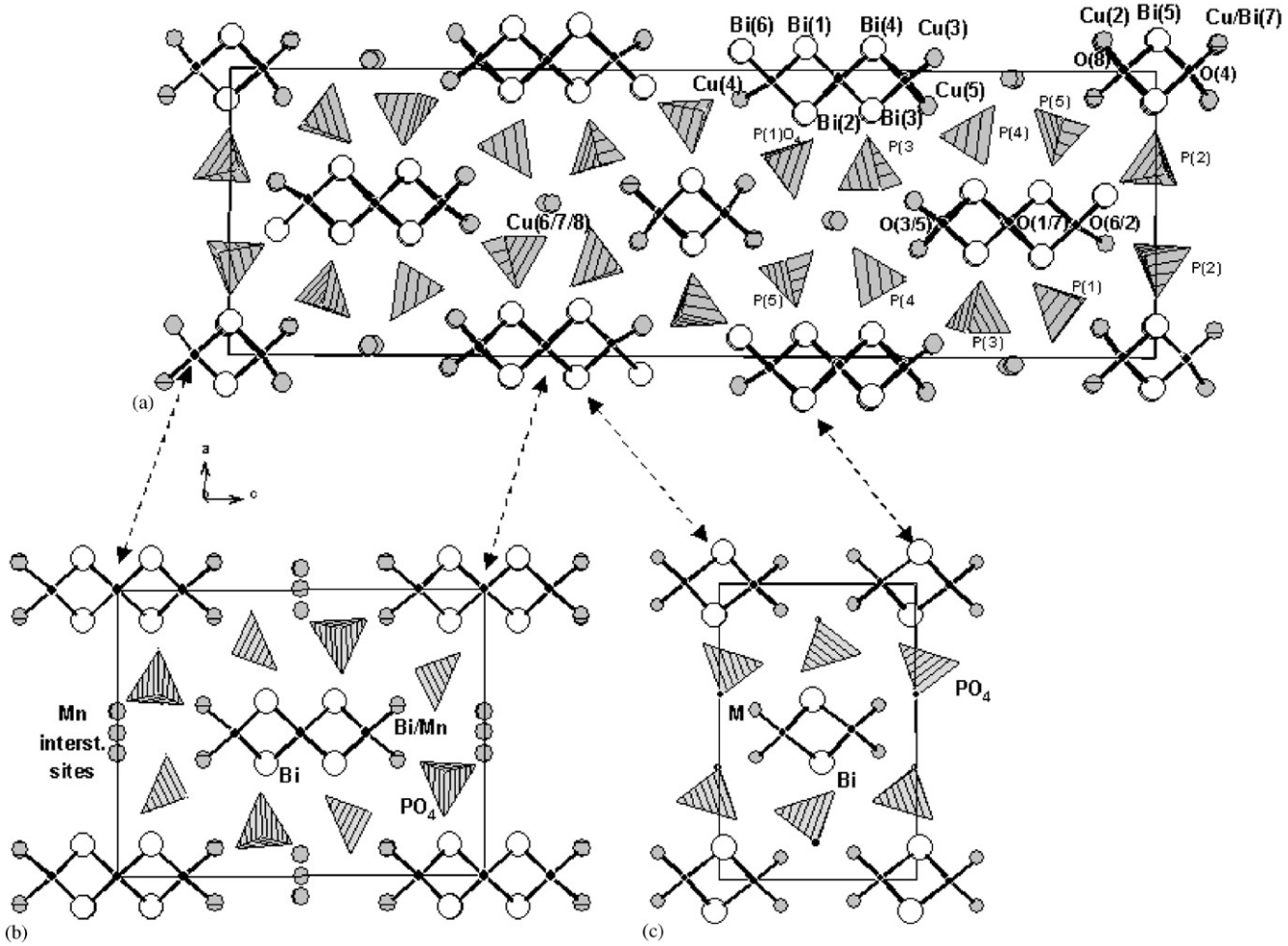

Fig. 3. (a) Projection along *b* of the $Bi_{6.2}Cu_{6.2}O_8(PO_4)_5$ ideal structure with the atomic label scheme. It evidences the 2- and 3-tetrahedra wide ribbons arrangement and the interstitial Cu(6)/Cu(7)/Cu(8) columns surrounded by PO_4 groups. The material can be considered as an intergrowth of (b) $Bi_{\sim 1.2}M_{\sim 1.2}PO_{5.5}$ showing 3-tetrahedra wide polycations only and (c) BiM_2PO_6 with 2-tetrahedra wide polycations only.

Physical evidences of inter-ribbon disorder have been recently shown by a strong important diffuse background in neutron diffraction pattern for this compound compared to the perfectly ordered $BiCu_2PO_6$ neutron diffraction pattern. This difference is not observed on XRD patterns implying the glassy-like nature of phosphate domains while the Bi-based ribbons framework is ordered. From the observation of these results and of additional materials [21], several general features for Bi^{3+}/M^{2+} oxyphosphates can be deduced:

1. A description based on the $O(Bi/M)_4$ tetrahedra linkage is well adapted evidencing the creation of infinite bidimensional polycations of variable width surrounded by phosphate groups.
2. Their size varies from the single chain (1-tetrahedon wide) to 2-, 3-tetrahedra wide ribbons. Their infinite extension leading to $[Bi_2O_2]^{2+}$ planes of the Aurivilius series, no size limit is expected (6-tetrahedra wide ribbons have just been found in a new compound to be published).
3. The ribbons cores are solely filled with Bi^{3+} while their edges can be Bi^{3+}, M^{2+} or Bi^{3+}/M^{2+} filled.
4. Only the mixed Bi^{3+}/M^{2+} occupancy for peripheral sites is responsible for a disorder in the inter ribbon space (PO_4 groups, sometimes forming tunnels with M^{2+} hosts).
5. Ribbons of different size can coexist in the same material (both 2- and 3-tetrahedra wide in the titled compound).

3.2. HREM images

3.2.1. [010] image

The [010] HREM image is interesting since it exhibits the size and the relative position of the ribbons with respect to each other. Images were simulated using the atomic coordinates from the X-ray average refined structure. A good agreement is obtained between the experimental (Fig. 4a) and calculated images, Fig. 4b, for a defocus of 100 Å and a thickness of 40 Å. Although the relation between the contrast and the atomic positions is not obvious at first glance, it is relatively easy to identify the ribbons: the contrast can be approximately described as formed from rows of white centered ovals and rows of white centered circles growing along the *a*-axis (Figs. 4a and b). The rows alternate along *c* within the –oval–oval–circle– sequence, Fig. 4c. According to the cations positions superimposition on an enlargement of the computed image (Fig. 4d) it was possible to understand the origin of the contrast. First, the ovals and circles contours are created by phosphorus and end of chains cations. Then, the long $[Bi_5Cu_3O_6]^{9+}$ cations are located between one oval and one circle subsequent to each other along *c* while the short $[Bi_{2.4}Cu_{3.6}O_4]^{6.4+}$ cations appear between two ovals.

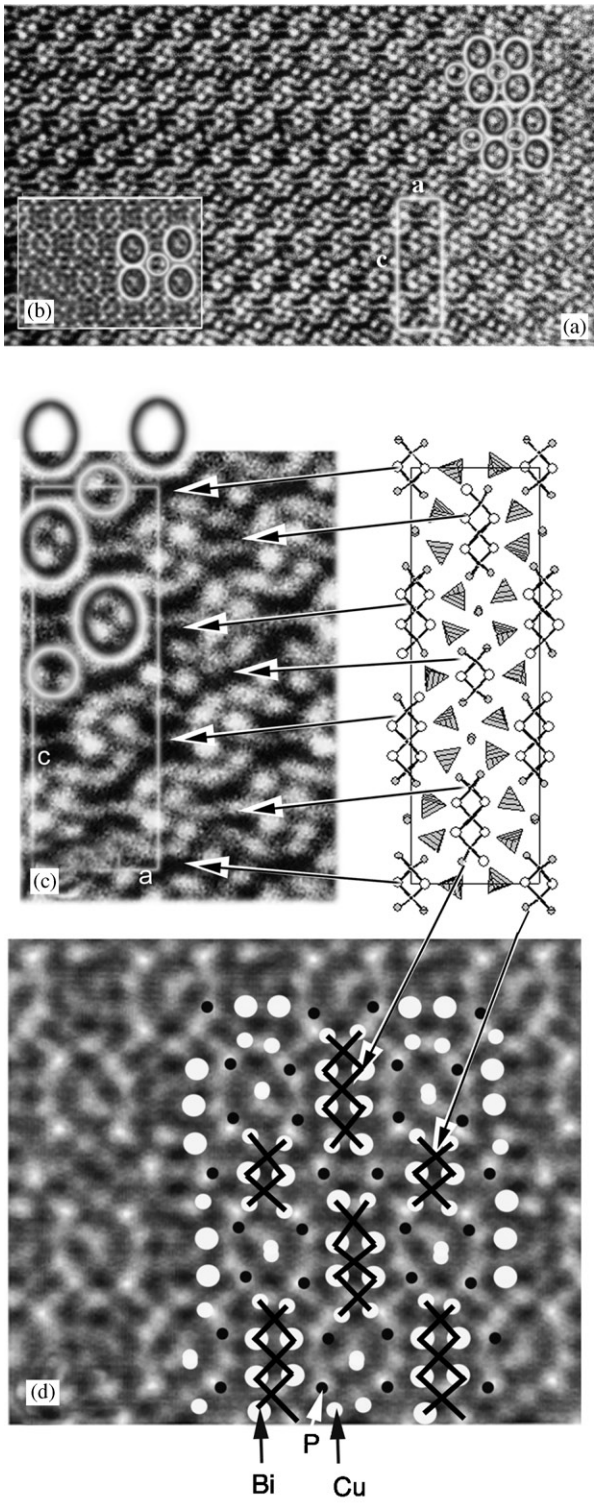

Fig. 4. (a) [010] HREM image and (b) calculated image for a defocus of 100 Å and a thickness of 40 Å. (c) For these conditions the positions of the different cations are superimposed on an enlargement of the computed image. (d) enlargement of a part of the image (a).

3.2.2. Ordering along b

In order to determine the origin of the partial ordering phenomenon detected in the ED study, an

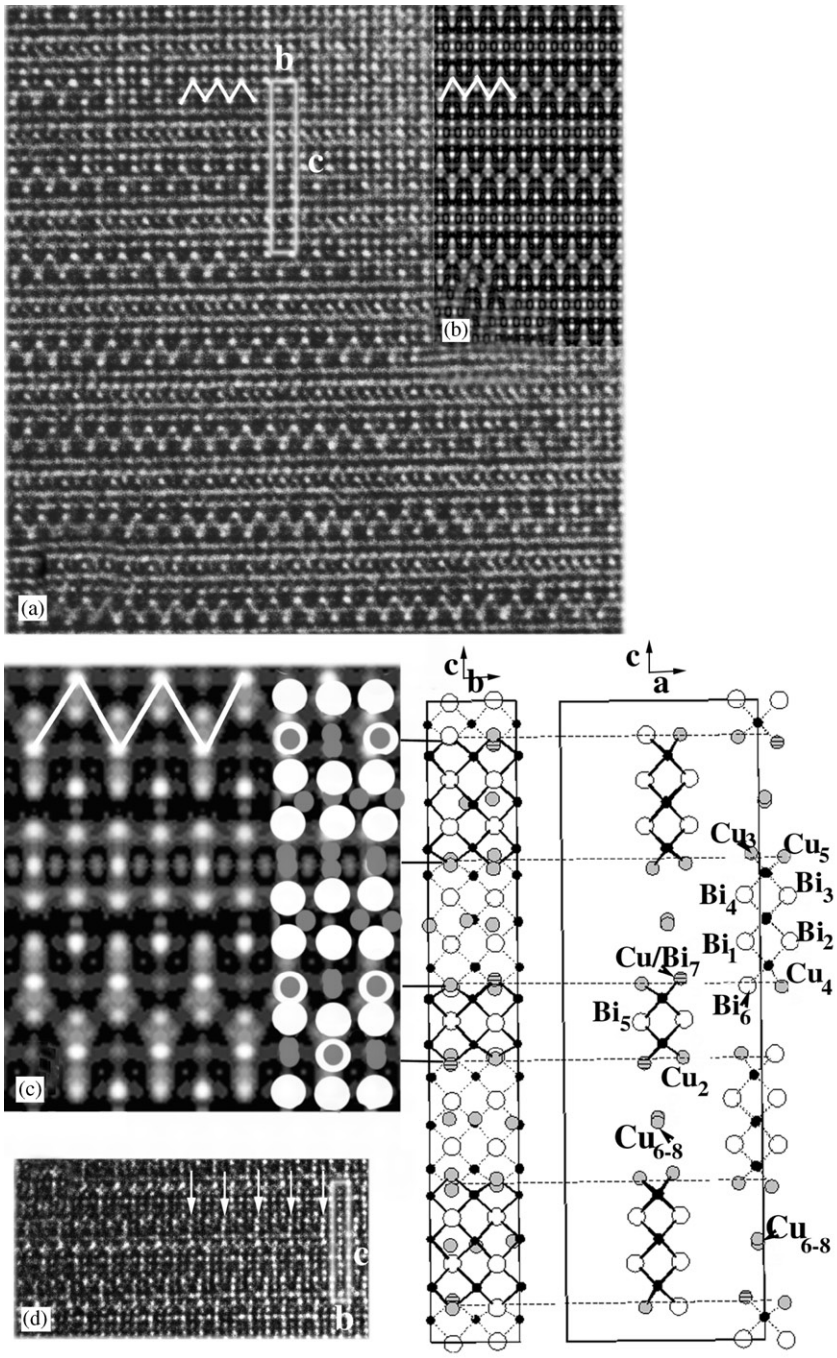

Fig. 5. (a) [100] HREM image of a thin part and (b) calculated image for a defocus of –675 Å and a thickness of 100 Å. (c) For these conditions the positions of the different cations are superimposed on an enlargement of the computed image. No trace of superstructure have been detected. (d) The superstructure is visible in a thicker part (arrows).

HREM study of the [100] zone axis has been investigated. No trace of *b*-doubling was observed on the HREM image of thin parts of crystals (Fig. 5a). The fitting between the experimental image and the calculated ones computed using the refined structure matches well for a defocus of –675 Å and a thickness of 100 Å (Fig. 5b). A characteristic of this contrast image is the white zigzag parallel to *b* (two per unit cell) delimited, as we can deduce from the cations superimposition of Fig. 5c, by the short ribbons location (Cu(2) and Cu/Bi(7) end of chains). The *b*-doubling is only visible in the thicker part of the crystal as indicated by white arrows in Fig. 4d.

A slight misorientation is necessary to observe it from a thin part of the crystal. Because this misoriented area is the only information available as regards the origin of

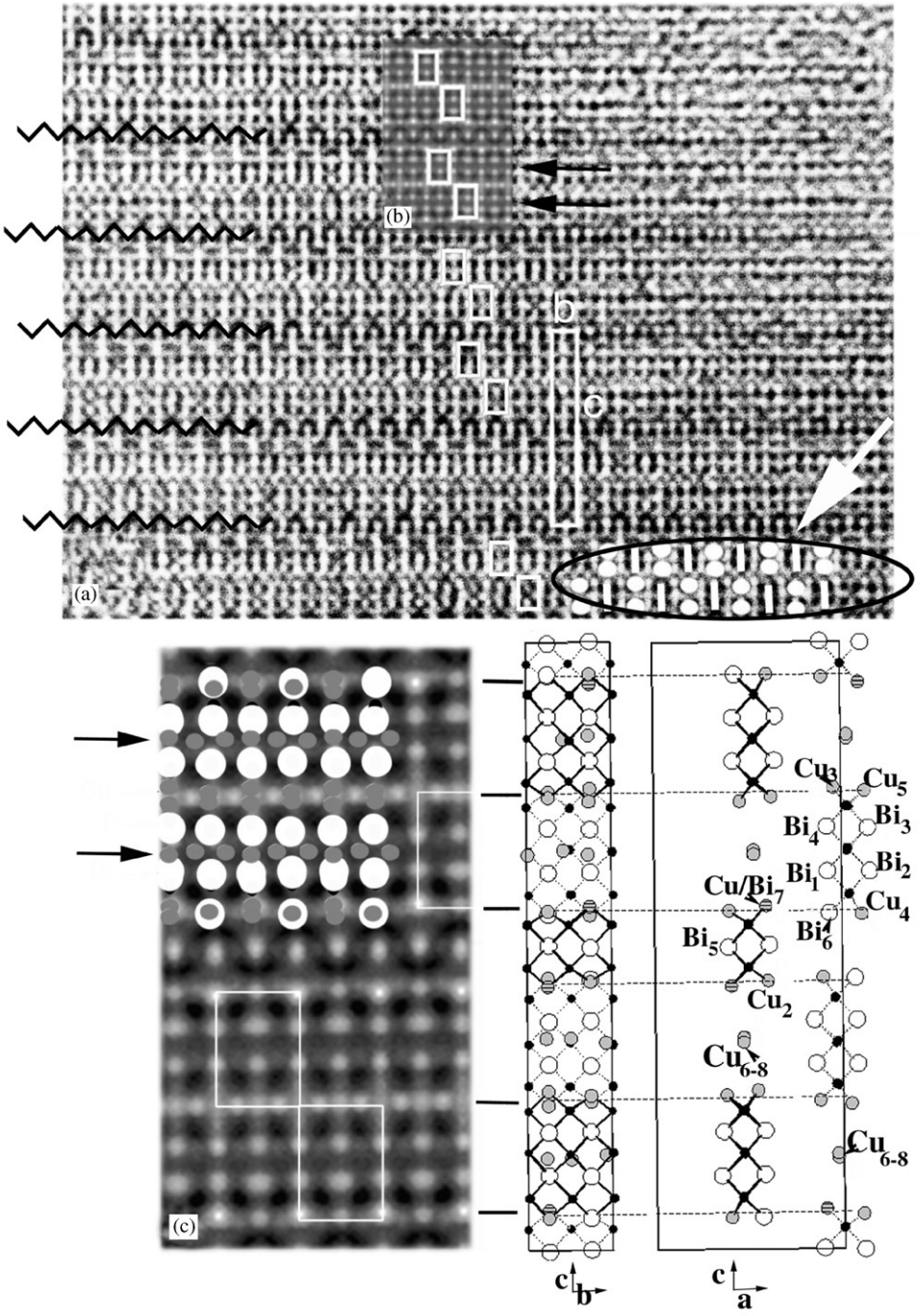

Fig. 6. (a) [100] HREM image of a thin part of a slightly disoriented crystal and (b) computed image for a thickness of 40 Å and a defocus of –50 Å. In accordance with the misorientation of the image, the superposition is not perfect. But the contrast of the experimental image as well as of the calculated one can be described by the alternation along *b* of two rows of rectangles separated with a black row in which white points form zigzag represented with black zigzag. The motif inside these rectangles is not always the same from one rectangle to each other (white arrow), what produce the superstructure phenomenon. Instead of having two points inside (white point in the figure) as indicated by the simulation, we have got one time out of two a line (white line in the figure). Black arrows indicate the layers where the superstructure occurs. (c) The different cations are superimposed on an enlargement of the computed image.

the superstructure, we have tried to analyze it. First, image simulations were computed using the average X-ray structure results, without any consideration of the *b*-doubling. A relatively good agreement has been obtained between experimental (Fig. 6a) and calculated images for a thickness of 40 Å and a defocus of –50 Å (Fig. 6b). According to the image misorientation, the agreement is not perfect. The contrast of the

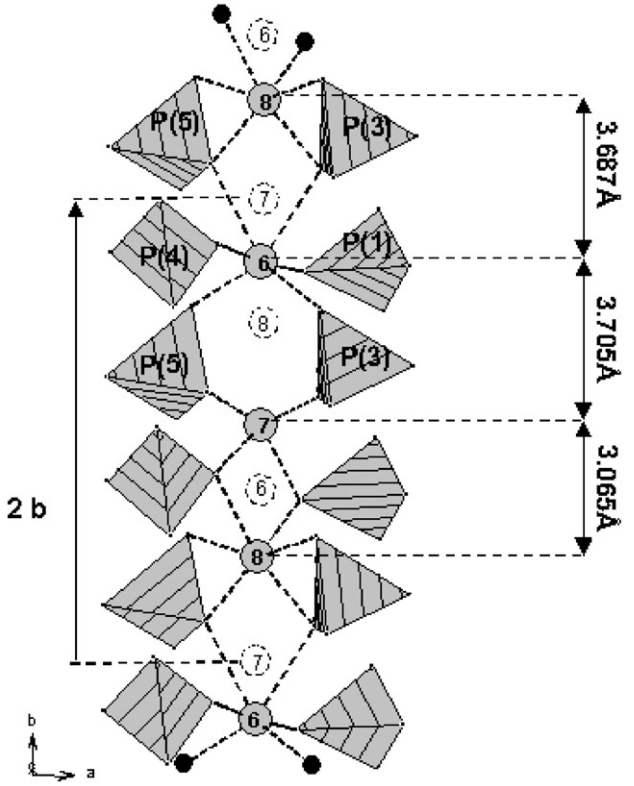

Fig. 7. The interstitial Cu(6)/Cu(7)/Cu(8) columns surrounded by PO_4 groups along *b*-axis.

experimental image as well as of the calculated one can be described by double rows of rectangle (schematically represented by white rectangle in Fig. 6a) growing along *b*. They are separated from each other by a zigzag of dark lines (schematically represented by black zigzag in Fig. 6a). Inside these rectangles, two different kinds of motifs alternate along *b* within a row, which produces the *b*-doubling. As highlighted at the bottom of Fig. 6a (see white arrow), it can be observed on some zones an ordering of two white points-centered rectangles (as predicted by the simulation, Fig. 6b) and white line-centered rectangles doubling the periodicity along *b*. What is the origin of such contrast changes?

Cu^{2+} Intra-tunnel ordering: In Fig. 6c, a projection of the cations positions of the structure, without any consideration of the superstructure, is superimposed on the calculated image. It is clear that the modification of contrast, namely the transformation of two points in one line occurs at the level of the middle of the rectangle (arrows in Fig. 6c) that corresponds to the level of the Cu(6)/Cu(7)/Cu(8) atoms. The Bi(1)–Bi(4) centering the long ribbons could also be involved, considering their projection inside the rectangles, but their participation in an ordering phenomenon is rather unlikely because of the unique Bi nature within these crystallographic sites. All the possible Cu(6) Cu(7) and Cu(8) positions are represented in the projected structure of Fig. 7. They are surrounded by PO4 groups whose oxygen corners form tunnel-like cavities occupied by the copper cations. Actually, the X-ray study leads to a partial occupancy close to 50% for these three sites. A proposition of ordering, based on reasonable Cu-Cu distances, is proposed. It involves a intra-tunnel Cu(6)–Cu(7)–Cu(8) sequence over two subsequent unit cells along *b* and respects the elimination of one copper out of two atoms. It is noticeable that some of the refined positions for oxygen of PO_4 groups lead to too short distances with interstitial copper atoms Cu(6)–Cu(8); therefore, it is important to keep in mind that this paper deals with the ideal crystal structure of $Bi_{6.2}Cu_{6.2}O_8(PO_4)_5$ mainly for two reasons: (i) geometrical restraints were applied to these oxygen atoms to respect a PO_4 tetrahedral configuration. (ii) Atoms P(3)–P(5) exhibit several PO_4 configurations (evidenced by several electronic residual density peaks around them) but only the most important was located. It also appears that phosphate groups playing a role on both peripheral ribbons and interstitial sites environments, a Cu/Bi(7) ordering would be correlated to the apparent intra-tunnel copper ordering. Images were simulated, for a perfect orientation, using this order proposition but the modification of contrast induced by such order is slight and only visible for some particular conditions of thickness and defocus. It would explain the lack of superstructure observation in thin part of oriented crystal (Fig. 5a).

Cu^{2+} Inter-tunnel ordering: As shown on the idealized contrast drawing at the bottom of Fig. 6a, for some parts of the crystal, the rectangle sequence (–line–2 points–line–) is shifted about *b* from one row to its neighbor within a double row. Considering the four Cu(6)/Cu(7)/Cu(8) tunnels per unit cell ($z_1 = 0.15$, $z_2 = 0.35$, $z_3 = 0.65$, $z_4 = 0.85$) an inter-tunnel ordering may be suggested strongly depending on the intra-tunnel ordering. The center of two adjacent rectangles being separated by $\Delta z = 0.20$, it appears that the tunnels would be coupled two by two (z_1/z_2 and z_3/z_4). The existence of both intra- and inter-tunnel ordering would be in good agreement with the observed [100] ZAP, Fig. 1b. The inter-tunnel is clearly evidenced by the *b*-doubling associated to diffuse lines parallel to *c*, that show the consequent partial inter-tunnel ordering.

Acknowledgments

The authors sincerely thank Professor G. Van Tendeloo for useful discussion, the EMAT laboratory (Antwerp, Belgium) for microscopy facilities, P. Shiv Halasyamani (Department of Chemistry, University of Houston, Texas) for second harmonic generation test and Ouassila Mebarki and Marie Colmont (LCPS) for their useful help in some experiments.

References

[1] M. Ketatni, Ph.D. Dissertation, Université des Sciences et Technologies de Lille, France, April 1995.
[2] G.B. Deacon, B.M. Gatehouse, G.N. Ward, Acta Crystallogr. C50 (1994) 1178.
[3] J. Huang, A.W. Sleight, J. Solid State Chem. 100 (1992) 170.
[4] J. Huang, Q. Gu, A.W. Sleight, J. Solid State Chem. 105 (1993) 599.
[5] I. Radosavljevic, J.S.O. Evans, A.W. Sleight, J. Solid State Chem. 137 (1998) 143.
[6] I. Radosavljevic, J.S.O. Evans, A.W. Sleight, J. Solid State Chem. 141 (1998) 149.
[7] I. Radosavljevic, J.S.O. Evans, A.W. Sleight, J. Alloys Compds. 284 (1999) 99.
[8] I. Radosavljevic, A.W. Sleight, J. Solid State Chem. 149 (2000) 143.
[9] F. Abraham, M. Ketatni, G. Mairesse, B. Mernari, Eur. J. Solid State Chem. 31 (1994) 313.
[10] N. Tancret, PhD Dissertation, Université des Sciences et Technologies de Lille, France, September 1995.
[11] A. Mizrahi, J.P. Wignacourt, H. Steinfink, J. Solid State Chem. 133 (1997) 516.
[12] A. Mizrahi, J.P. Wignacourt, M. Drache, P. Conflant, J. Mater. Chem. 5 (1995) 901.
[13] M. Ketatni, B. Mernari, F. Abraham, O. Mentre, J. Solid State Chem. 153 (2000) 48.
[14] S. Giraud, A. Mizrahi, M. Drache, P. Conflant, J.P. Wignacourt, H. Steinfink, Solid State Sci. 3 (2001) 593.
[15] I. Radosavljevic, J.A.K. Howard, R.L. Whithers, J.S.O. Evans, Chem. Commun. 19 (2001) 1984.
[16] F. Abraham, M. Ketatni, Eur. J. Solid State Inorg. Chem. 32 (1995) 429.
[17] M. Ketatni, F. Abraham, O. Mentre, Solid State Sci. 1 (1999) 449.
[18] S. Nadir, J.S. Swinnea, H. Steinfink, J. solid State Chem. 148 (1999) 295.
[19] X. Xun, S. Uma, A. Yokochi, A.W. Sleight, J. Solid State Chem. 167 (2002) 245.
[20] X. Xun, S. Uma, A.W. Sleight, J. Alloys Compds. 338 (2002) 51.
[21] F. Abraham, O. Cousin, O. Mentre, El M. Ketatni, J. Solid State Chem. 167 (2002) 168.
[22] "SAINT+" ver. 5.00, Bruker Analytical X-ray Systems, 2001.
[23] SADABS V2.03, Bruker/Siemens Area detector absorption and other corrections, 2001.
[24] Mac Tempas, Roard Kilaas, Total resolution, Berkeley.
[25] S.K. Kurtz, T.T. Perry, J. Appl. Phys. 39 (1968) 3798.
[26] Y. Porter, K. Min Ok, N.S.P. Bhuvanesh, P. Shiv Halasyamani, J. Solid State Chem. 13 (2001) 1910.
[27] K. Min Ok, N.S.P. Bhuvanesh, P. Shiv Halasyamani, J. Solid State Chem. 161 (2001) 57.
[28] J.P. Morniroli, J.W. Steeds, Ultramicroscopy 45 (1992) 219–239.